

Printable, stretchable metal-vapor-desorption layers for high-fidelity patterning in soft, freeform electronics

Received: 6 December 2023

Accepted: 8 August 2024

Published online: 22 August 2024

 Check for updatesSujin Jeong ^{1,5}, Hyungsoo Yoon ^{1,5}, Lukas Felix Michalek ², Geonhee Kim¹,
Jinhyoung Kim³, Jiseok Seo ¹, Dahyun Kim¹, Hwaeun Park¹,
Byeongmoon Lee ⁴ ✉ & Yongtaek Hong ¹ ✉

High-fidelity patterning of thin metal films on arbitrary soft substrates promises integrated circuits and devices that can significantly augment the morphological functionalities of freeform electronics. However, existing patterning methods that decisively rely on prefabricated rigid masks are severely incompatible with myriad surfaces. Here, we report printable, stretchable metal-vapor-desorption layers (s-MVDLs) that can enable high-fidelity patterning of thin metal films on freeform polymeric surfaces. The printed rubbery matrix with highly mobile chains effectively repels various metal vapors from the surface and inhibits their condensation, thereby allowing selective metal deposition. The s-MVDLs are printed by direct ink writing techniques, enabling customizable and scalable thin metal patterns ranging from the micrometer to millimeter scale with high fidelity. Furthermore, the superior stretchability and mechanical robustness of the s-MVDLs allow highly compliant deformation along the substrates, enabling the construction of unconventional circuits and devices on multi-curvature, non-developable, and stretchable surfaces.

Thin metal films on arbitrary soft, curvilinear surfaces offer additional functionalities for next-generation freeform electronics, such as wearable systems for optoelectronics and wireless communications^{1–3} and bioinspired sensor arrays for therapeutics and health monitoring^{4–6}. Their high-fidelity patterns with minimized feature sizes significantly augment the resolution of unconventional electronic systems, and elaborately designed patterns can greatly broaden their morphological functionalities⁷. Vacuum-assisted thermal evaporation, a basic method for the deposition of thin metal films, generally ensures high conductivity and low surface roughness with nanoscale thickness^{8,9}. However, the patterning process in this method, which relies on prefabricated stiff shadow masks, disrupts favorable employment on uneven or sticky surfaces. Even if an ultrathin flexible

mask¹⁰ or elastomeric mask^{11,12} can be temporarily applied to accommodate compliant deformation, the rigorous design criteria of these components makes them impractical and they are difficult to reuse, limiting the feasibility of their use in this process. Although some subtractive methods (e.g., photolithography, laser ablation, sacrificial layer) have been suggested^{13–15}, the high thermal energies or chemical reactions that can occur during the patterning process can irreversibly damage soft substrates; thus, these methods do not represent a universal solution.

Spontaneous area-selective deposition using metal-vapor-desorption layers (MVDLs) has been proposed as an alternative strategy for thin metal patterning^{16–20}. MVDLs effectively impede the growth of metal films during thermal evaporation by suppressing

¹Department of Electrical and Computer Engineering, Inter-University Semiconductor Research Center (ISRC), Seoul National University, Seoul 08826, Korea.

²Department of Chemical Engineering, Stanford University, Stanford, CA 94305, USA. ³Smart Sensor Research Center, Korea Electronics Technology Institute (KETI), Seongnam 13509, Korea. ⁴Department of Electrical Engineering and Computer Science, Daegu Gyeongbuk Institute of Science and Technology (DGIST), Daegu 42988, Korea. ⁵These authors contributed equally: Sujin Jeong, Hyungsoo Yoon. ✉ e-mail: byeongmoon@dgist.ac.kr; yongtaek@snu.ac.kr

the condensation of metal vapor on the surface, while thin metal films exclusively grow in areas without these functional layers, resulting in the desired patterns. Several studies have reported the effectiveness of MVDLs, particularly those based on photochromic diarylethene (DAE) and fluorinated polymers, in modulating the condensation of metal vapors. For instance, Varagnolo *et al.*¹⁹ reported that fluorinated polymers, such as a trichloro(1*H*,1*H*,2*H*,2*H*-perfluorooctyl) silane (FOTS) and semi-crystalline poly(vinylidene fluoride-co-hexafluoropropylene) (c-PVDF-HFP), resisted metal condensation, demonstrating the patterning of silver and copper thin films for the first time. Lee *et al.*²¹ further explored the fluorinated polymer blended with small molecules to enhance uniformity and thickness controllability. A poly(3,3,4,4,5,5,6,6,7,7,8,8,9,9,10,10,10-heptadeca-fluorodecyl methacrylate) (PFDMA):FOTS blend features a low condensation coefficient for silver, constructing a fused Ag nano-networks. These patterned thin metal films were utilized for transparent electrodes or flexible optoelectronic devices, which have led to the exploration of various maskless processes using MVDLs. However, two major drawbacks prevent the employment of MVDLs for soft, freeform substrates. First, current methodologies for depositing MVDLs rely on prefabricated physical templates, which impede pattern formation onto curved surfaces, customizable designs, and uniform deposition over large areas. Second, insufficient desorption characteristics result in low deposition selectivity, leading to formation of metal residues on the MVDL surface and a decrease in optical transmittance²¹. While a slow deposition rate can be introduced during thermal evaporation to enhance the desorption properties^{16,22}, it is impractical in terms of low process throughput. Even if additional condition is refined, the evaporation thickness permitted for desorption has been restricted to 100 nm for metal species with low intrinsic vapor pressure²³. In addition to these limitations, the softness of desorption materials is another critical concern for their reliable application to curvilinear or deformable substrates. The softness of MVDLs allows for compliant deformation along the substrates, facilitating effective metal desorption even on arbitrarily shaped surfaces unless the MVDL is physically disconnected. Previous studies have utilized MVDLs in flexible electronics^{19,21,22}, but the softness of MVDLs has not yet been explored. Therefore, the development of MVDLs universally compatible with various metal species and soft, polymeric substrates, as well as the establishment of appropriate patterning methods, is highly desired.

Here, we report high-fidelity patterning of thin metal films through the use of printable, stretchable MVDLs (s-MVDLs) that allow in situ metallization onto arbitrary, non-planar platforms. A rubbery matrix of elastomer poly(vinylidene fluoride-co-hexafluoropropylene) (e-PVDF-HFP), as a principal constituent of the s-MVDLs, is characterized by its highly mobile chains and weak interaction with metal atoms, which synergistically contributes to repelling most of the metal vapors with an ultralow condensation ratio (<2%). This excellent desorption capability effectively prevents the deposition of various metal species (Ag, Cu, Au, etc.) while maintaining their inherent optical transparency after metal deposition. The rheological properties of the s-MVDL solution are modulated for direct ink writing, allowing highly customizable and scalable patterning of s-MVDLs using various printing techniques, such as pneumatic dispensing or electrohydrodynamic (EHD) methods. During thermal evaporation, the metal vapors are exclusively deposited on the s-MVDL-free regions, achieving thin metal films with desired patterns ranging from the microscale ($\sim\mu\text{m}$) to macroscale ($\sim\text{mm}$) while maintaining high conductivity and low surface roughness. The boundary region of the metal films exhibits a steep profile with tapered regions less than $1\mu\text{m}$ in width at the patterned edge, ensuring a high-fidelity metallization with a minimum feature size of $<8\mu\text{m}$. Furthermore, the intrinsic stretchability (>1000%) and mechanical robustness of s-MVDLs enable highly

compliant deformation along 3D curvilinear surfaces or arbitrary shapes, allowing in situ selective metallization on multi-curvature or elastomeric substrates. To fully exploit these patterned thin metal films on diverse surfaces, wireless power transfer to drive microscale light-emitting diodes (LEDs), organic light-emitting diodes (OLEDs), and a stretchable LED array is demonstrated. The high-fidelity, seamless patterning of thin metal films on complex, non-planar substrates and the efficient desorption properties compatible with various metal species highlight our metallization strategies for free-form electronics.

Results

Selective metal vapor deposition using printable s-MVDLs

Figure 1a illustrates the process flow for patterning thin metal films by employing a printable s-MVDL. The patterning process involves (i) printing the s-MVDL ink and (ii) subsequently applying thermal evaporation without a mask, forming (iii) selectively patterned thin metal films. Optional processes such as the cross-linking of s-MVDL ink and surface treatment are selectively adjusted depending on the substrate type (Supplementary Table 1). Notably, the experiments were mostly conducted using Ag metal sources unless otherwise specified. For the s-MVDL material, an optically transparent solution was prepared by dissolving e-PVDF-HFP with cross-linking agents in propylene glycol monomethyl ether acetate (PGMEA). The concentration of e-PVDF-HFP was adjusted to obtain the required rheological properties, specifically viscosity and surface tension, necessary for facile extrusion using direct ink writing techniques. The formulated s-MVDL ink was applied under ambient conditions with printing equipment, such as a pneumatic dispenser or EHD printer. This compatibility with various printing systems allows customizable and scalable patterning, constructing elaborate patterns without a pre-designed physical template. When the substrate with the printed s-MVDL was exposed to metal vapor flux in a high-vacuum chamber ($<10^{-6}$ Torr), the growth of thin metal films was suppressed on the surface of the printed s-MVDL, as it effectively repelled the metal vapor. However, in the s-MVDL-free region, thin metal films were successfully constructed through continuous nucleation of metal atoms, achieving the selective deposition of thin metal films in desired patterns.

To experimentally evaluate the desorption phenomena, a slit structure, serving as a collecting plate for metal vapor, was employed above the s-MVDL-coated glass substrate (Supplementary Fig. 1). When Ag was thermally evaporated, the metal vapor that passed through the slit opening was not deposited onto the target substrate, maintaining the substrate transparency without Ag detection. Instead, Ag atoms were detected on the collecting plate located above the target substrate by energy-dispersive X-ray spectroscopy (EDS), rendering the collecting plate opaque around the slit opening region. These results indicate that the s-MVDL effectively inhibited thin metal film growth by repelling the metal vapor. Furthermore, EDS maps of the printed s-MVDL and patterned Ag thin films showed no Ag in the s-MVDL regions, proving the selective deposition of metal vapor on the s-MVDL-free regions (Fig. 1b). In addition to Ag, other metal species, including Mg, Ca, Cu, and Au, were selectively deposited in patterns depicting their respective atomic information in the periodic table (Fig. 1c). Although the selective deposition of Au through the existing MVDL-based methods has been challenging due to its inherently low vapor pressure^{18,24}, the universal compatibility of our method with various metal species, including Au atoms, highlights its desorption capabilities. Furthermore, the cross-linked s-MVDL is highly stretchable, enduring a strain of approximately 1000% without fracture (Fig. 1d). This deformability allows compliant deformation in conjunction with underlying substrates. Therefore, selective deposition of thin metal films on versatile platforms beyond 2D planar substrates becomes feasible, allowing conformal integration of thin metal films into 3D or deformable domains (Fig. 1e).

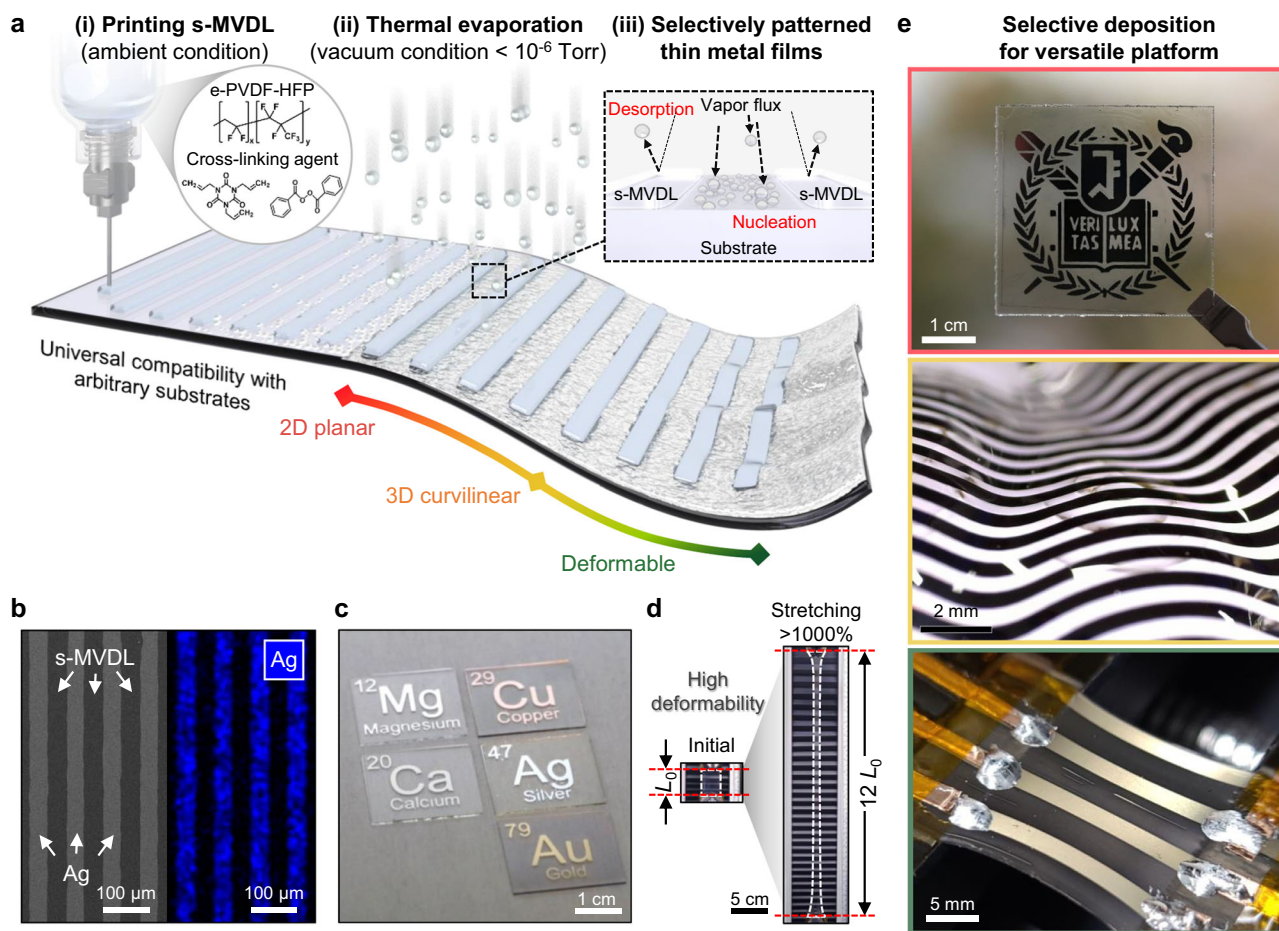


Fig. 1 | Overview of s-MVDL-assisted selective metal vapor deposition.

a Schematic illustration of s-MVDL-assisted selective metal vapor deposition, including printing and sequential thermal evaporation. The inset shows the desorption of metal vapor in the printed s-MVDL region and its selective deposition on the s-MVDL-free region. **b** field-emission scanning electron microscopy (FE-SEM) image of Ag thin films patterned using the printed s-MVDL and the corresponding

EDS map image. **c** Photograph of patterned thin metal films from various metal sources (Mg, Ca, Cu, Ag, and Au). All of the metal sources were thermally evaporated to form films with a thickness of 100 nm, except for Au ($t = 50$ nm). **d** Photograph of a free-standing s-MVDL with high stretchability (>1000%). **e** Photographs of patterned thin metal films achieved through s-MVDL-assisted selective metal vapor deposition on versatile platforms.

Metal-vapor-desorption property of s-MVDLs

In the thermal evaporation process, the condensation of metal vapor is fundamentally determined by the interplay of the cohesive force between metal atoms and the adhesive force between the surfaces and metal atoms⁸. Apart from the cohesive term associated with the intrinsic properties of metal species, the adhesive force must be weakened to facilitate the desorption of metal vapor. When focusing on the interaction between metal vapors and polymers, the dynamic molecular motion in polymer chains could supply kinetic energy to metal atoms adsorbed on the surface^{25,26}. These metal atoms with high mobility undergo fluctuations in the adhesive energy barrier, resulting in their desorption from the surface²⁴. In this regard, the metal-vapor-desorption phenomenon is critically influenced by the characteristics of the surface. Specifically, a liquid-like surface featuring a highly mobile chain associated with a low glass transition temperature (T_g) and its weak interactions with metal vapors related to a low dispersive component of surface energy (γ_D) are particularly critical in facilitating the efficient desorption of metal atoms (Fig. 2a)²⁴.

Based on the above considerations, s-MVDLs, primarily composed of a fluoroelastomer e-PVDF-HFP, emerge as a favorable candidate for metal-vapor desorption. This material is characterized by a high molar ratio of soft and amorphous HFP contents, and its distinct fluorine-rich molecular structure features high chain mobility, facilitating weak interactions with foreign materials²⁷. In particular, the steric hindrance

by the $-\text{CF}_3$ pendant group in the HFP moiety offers an irregularity in polymer backbone, leading to a low crystallinity^{28–30}. The rubbery matrix of e-PVDF-HFP results in dynamic molecular motion and low intermolecular interaction, proven by a low T_g of -24 °C. This unique feature enables metal-vapor desorption even at room temperature. Furthermore, the fluorocarbon bonds (C–F) of the e-PVDF-HFP layer, offering a low γ_D of 12.81 mJ m^{-2} , substantially weaken its interaction with metal vapors. Consequently, the s-MVDL, with a low T_g below room temperature and low γ_D (<20 mJ m^{-2}), can exhibit better desorption properties than the previously reported MVDLs (Fig. 2b).

To experimentally validate the desorption performance, a comparative analysis was conducted with the previously reported MVDLs available^{19,24}. The functional materials of c-PVDF-HFP, polydimethylsiloxane (PDMS), and FOTS were selected as the control group, exhibiting distinct properties in terms of γ_D and T_g . Notably, c-PVDF-HFP differs from e-PVDF-HFP, the main component of s-MVDL, in terms of the degree of crystallinity determined by the molar ratio of vinylidene fluoride (VDF) and hexafluoropropylene (HFP)^{27,31}. Detailed descriptions of the coating methods for each MVDL are provided in the Method section. Moreover, variations in desorption performance may occur depending on the quality and thickness of the deposited film, potentially differing from outcomes reported in previous studies. In Fig. 2c, suppressed thin film growth compared to that on the bare glass can be observed through a difference in optical transparency. The

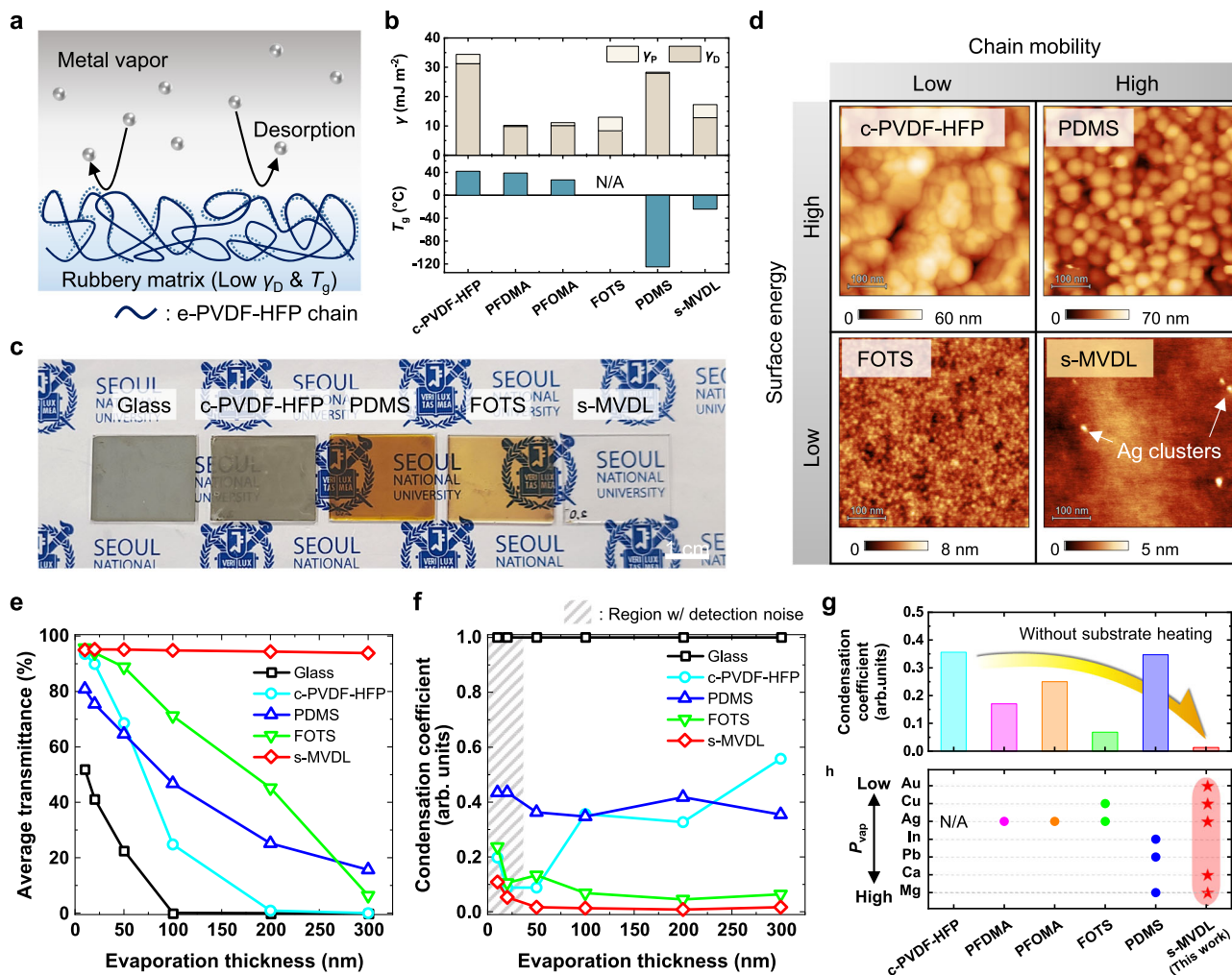


Fig. 2 | Desorption property of s-MVDL. **a** Schematic illustration of the desorption phenomenon induced by the active motion of e-PVDF-HFP chains and the weak interaction between metal vapor and e-PVDF-HFP. **b** Surface energy (γ) and glass transition temperature (T_g) of various MVDLs. The surface energy is the sum of polar (γ_p) and dispersive components (γ_D). **c** Photographs of the glass substrates coated with nothing, c-PVDF-HFP, PDMS, FOTS, and s-MVDL after thermal evaporation of Ag ($t = 100$ nm) and **(d)**, the corresponding AFM images. The images

and color bars represent height data for each sample. **e** Average optical transmittance as functions of the evaporation thickness. The average transmittance was obtained in the wavelength range from 400 nm to 800 nm. **f** Condensation coefficient as functions of the evaporation thickness. The shaded region shows inconsistent trends due to detection noise from low EDS intensity. Comparison of the **(g)**, condensation coefficient and **(h)**, patternable metal species of the previously reported MVDLs. P_{vap} represents the intrinsic vapor pressure of the metal species.

glass with the s-MVDL was completely transparent owing to its superior desorption repelling most of the Ag vapor and the intrinsic transparency of s-MVDLs (Supplementary Fig. 2). In atomic force microscopy (AFM) images, the difference in film growth was more clearly observed (Fig. 2d). First, a higher chain mobility led to the formation of nanoparticle-like Ag clusters, while a lower chain mobility resulted in a film-like structure with densely packed Ag grains. Notably, FOTS underwent a slow polymerization, activated by a small amount of moisture in the processing solvent, thus forming an ultrathin layer of only a few nanometers grafted onto the rigid glass surface^{19,24}. While coating a denser and thicker layer of FOTS can potentially enhance desorption based on its highly mobile chain with fluorocarbon moieties¹⁹, the chain movement was confined to the several nanometer scales in our experimental results, resulting in the formation of small-sized grains. Second, the dispersive surface energy played a significant role in determining the absolute quantity of Ag atoms condensed on the surface. c-PVDF-HFP and PDMS, characterized by relatively higher surface energy, exhibited a substantial amount of Ag on their surfaces, whereas FOTS and the s-MVDL with lower surface energy, showed only a minute amount. Overall, the synergistic combination of sufficiently active chain mobility and low dispersive surface energy in the s-MVDL

contributed to its remarkable desorption properties. Only a few Ag clusters, with sizes of several hundred nanometers, were sparsely distributed on the s-MVDL. Therefore, this material holds great promise as a highly efficient desorption layer for selective metal vapor deposition.

A further comprehensive comparison was carried out through a quantitative analysis of the optical transparency and the amount of condensed Ag content. Figure 2e presents the average optical transmittance of the glass substrate with different coating materials as a function of evaporated thickness. In contrast to a gradual decrease in optical transparency observed in the other samples, the s-MVDL consistently maintained a high transparency level of over 93% even up to an evaporation thickness of 300 nm. Figure 2f shows the condensation coefficient as a function of evaporation thickness. The condensation coefficient was determined by normalizing the Ag peak intensity of the EDS spectrum with respect to the corresponding intensity of bare glass at the same thickness, representing a relative amount of condensation at each thickness. The shaded region in the plot corresponds to an evaporation thickness below 50 nm, where the low EDS intensity with detection noise led to inconsistent condensation coefficient values. Except for the shaded region, the condensed Ag content decreased in

the order of c-PVDF-HFP \approx PDMS > FOTS > s-MVDL, exhibiting the superior desorption property of the s-MVDL. The lowest amount of Ag was condensed on the surface of the s-MVDL, with a ratio of less than 2%. This low condensation value highlights its competitive desorption performance compared to other control groups and the previously reported materials under conditions without substrate heating in the evaporation process (Fig. 2g). Furthermore, this low condensation ratio can be achieved without the need for thermal cross-linking of s-MVDL, showing the compatibility of our method to low-temperature process (Supplementary Fig. 3).

To improve the condensation coefficient further, studies have been reported with substrate heating during thermal evaporation. For example, near-zero condensation coefficients were achieved using PFDMA at a substrate temperature of 190 °C²². More recently, a poly(3,3,4,4,5,5,6,6,7,7,8,8,8-tridecafluorooctylmethacrylate) (PFOMA) has lowered process temperatures to 90 °C, reducing the thermal exposure to substrates²⁰. Despite these advancements, minimizing heat exposure remains crucial for ensuring compatibility with heat-sensitive materials and preserving thin film integrity, as substrate heating can lead to the formation of discontinuous films due to metal adatom aggregation^{32,33}. When the glass substrate was heated during thermal evaporation, the desorption property was enhanced with increasing substrate temperature (Supplementary Fig. 4). However, unless adequate seed layers or surface modification to the target surface is introduced^{19,20}, deposited metal vapors construct island-like morphologies, which could degrade electro-optical characteristics. Therefore, s-MVDL, ensuring a low condensation ratio and reliable thin film quality, offers distinct advantages for selective patterning thin metal films. Furthermore, its efficient desorption property provides a comprehensive process window for diverse deposition conditions (Supplementary Fig. 5). This property not only applies to Ag, but also extends to Au, which has low intrinsic vapor pressure, demonstrating superior deposition selectivity with high average optical transmittance (>92% @ 50 nm, >86% @ 100 nm) and a low condensation coefficient (<0.1) (Supplementary Fig. 6 and Supplementary Fig. 7). These results reveal the feasibility of patterning various metal species using s-MVDL (Fig. 2h and Supplementary Table 2).

Additionally, the s-MVDLs with Ag deposited up to an evaporation thickness of 300 nm entirely maintained electrical insulation, with a resistance of over 200 M Ω , exceeding the measurable range of the instrument (Supplementary Fig. 8). In contrast, the bare glass with deposited Ag became electrically conductive as the deposition thickness exceeded the percolation threshold, thus decreasing the sheet resistance from 75 Ω sq⁻¹ to 0.06 Ω sq⁻¹. These results support that the s-MVDL ensures sufficient desorption characteristics that can simultaneously achieve electrical insulation between conductive paths.

High-fidelity and scalable patterning of thin metal films

Printed s-MVDLs with elaborate patterns can spatially define the growth and non-growth regions of metal vapors based on the excellent desorption properties of the s-MVDL. For stable printing of s-MVDL ink, the ink concentration was designed to be compatible with various printing systems (Supplementary Fig. 9). For instance, an ink with a 10 wt% e-PVDF-HFP concentration, resulting in a viscosity and surface tension of 52.7 cP and 25.8 mN m⁻¹, respectively, was selected for printing with a pneumatic dispenser. At lower concentrations, such as below 10 wt%, the ink tended to leak from the nozzles and excessive ink volumes caused undesirable spreading in the printed pattern. On the other hand, an ink with a 5 wt% e-PVDF-HFP concentration, resulting in a viscosity and surface tension of 11.1 cP and 26.3 mN m⁻¹, respectively, was chosen for printing with an EHD printer. The lower concentration facilitated the jetting of s-MVDL ink with dielectric properties, whereas higher concentrations caused nozzle clogging. The feature size and resolution of the s-MVDL can accommodate wide ranges, from macroscale (~mm) to microscale (~ μ m), depending on

the utilized printing system³⁴. Fig. 3a shows printed s-MVDL patterns with linewidths of ~400 μ m and ~50 μ m obtained using a pneumatic dispenser and an EHD printer, respectively. The linewidths were further reduced to ~200 μ m and ~30 μ m by adjusting the printing parameters, such as the movement speed and the inner diameter of the nozzle (Supplementary Fig. 10). As the linewidth of the s-MVDL determined the gap between the thin metal films, scalable printing of the s-MVDL enabled the patterning of thermally evaporated thin Ag films at various scales ranging from millimeters to several tens of micrometers. The surface profiles of the as-printed s-MVDL and that after Ag evaporation were measured by AFM. While as-printed s-MVDL maintained its profiles before and after Ag thermal evaporation, the s-MVDL-free areas were filled with Ag films of uniform thicknesses, achieving selective metallization (Fig. 3b). This indicates that much fewer metals were deposited on the s-MVDL surface than on the substrate. Subsequently, as an optional process, the printed s-MVDL patterns could be further removed while preserving the intact Ag thin films by rinsing with acetone. The surface profiles of the remaining Ag thin films indicate that sharp edges were established near the s-MVDL boundaries. Therefore, highly customizable, scalable, and accurate patterning of thin metal films can be achieved through our approach without complex lithographic processes.

The edge profiles of the evaporated Ag thin films were further investigated in detail. In the thermal evaporation process, a shadow effect occurs when the evaporated metal vapor traveling in a straight trajectory is interrupted by physical obstacles^{35–37}. For example, when a shadow mask ($t = 100 \mu$ m) was employed, a tapered region with a width of ~30 μ m was observed at the edge because of the shadow effect, which caused insufficient deposition along the opening edges (Supplementary Figs. 11a and 11b). As the feature size is further reduced to the micrometer scale, the overall pattern can fall within the shadow zone, resulting in low accuracy, low fidelity, and poor uniformity of the evaporated thin films³⁸. In contrast, in the maskless patterning utilizing the s-MVDL, the printed s-MVDL with a pattern edge thickness of less than 100 nm allowed sufficient travel paths for the metal vapor, thus producing relatively uniform Ag films with improved edge profiles (Supplementary Figs. 11c and 11d). However, a transition zone, defined as a region from the boundary to the point where the thickness becomes uniform, could still be observed, which degraded the pattern fidelity in finer patterns at a scale of a few micrometers. (Fig. 3c).

The surface profiles of Ag thin films deposited on the bare glass substrates with printed s-MVDLs were observed using AFM (Fig. 3d; surface profiles of the as-printed s-MVDLs in Supplementary Fig. 12). The profile of the as-printed s-MVDL shows that the printed ink exhibited uneven spreading on the bare glass substrate, forming tails with thicknesses of tens of nanometers near the boundary. Notably, as the thickness of the s-MVDLs decreased below 20 nm, the desorption properties were reduced, as indicated by the decrease in the optical transmittance of the thin s-MVDLs after Ag evaporation (Supplementary Fig. 13). Therefore, the Ag film growth was affected by the undesirable spread of the s-MVDL ink, resulting in a pattern edge with a gradual slope defined as a transition zone (L_1) of ~5 μ m and poor surface morphology with porous holes. In particular, because the fidelity of the patterned electrodes critically depends on their edge profiles, a reduction in the transition zone is needed for fine metal patterns requiring high fidelity and smaller feature sizes. When 3-aminopropyltriethoxysilane (APTES) was applied to the substrate, the spreading of the s-MVDL ink was effectively reduced through contact line pinning, resulting in a reduced transition zone (L_2) of less than 2 μ m. Furthermore, when FOTS was applied, ink spreading was impeded by dewetting (Supplementary Fig. 14); therefore, the low-thickness region of the s-MVDL was minimized, resulting in a further reduction in the transition zone (L_3) to less than 1 μ m.

By controlling the spreading of the s-MVDL ink, Ag thin films with ultra-sharp edges were established, achieving Ag electrodes with a

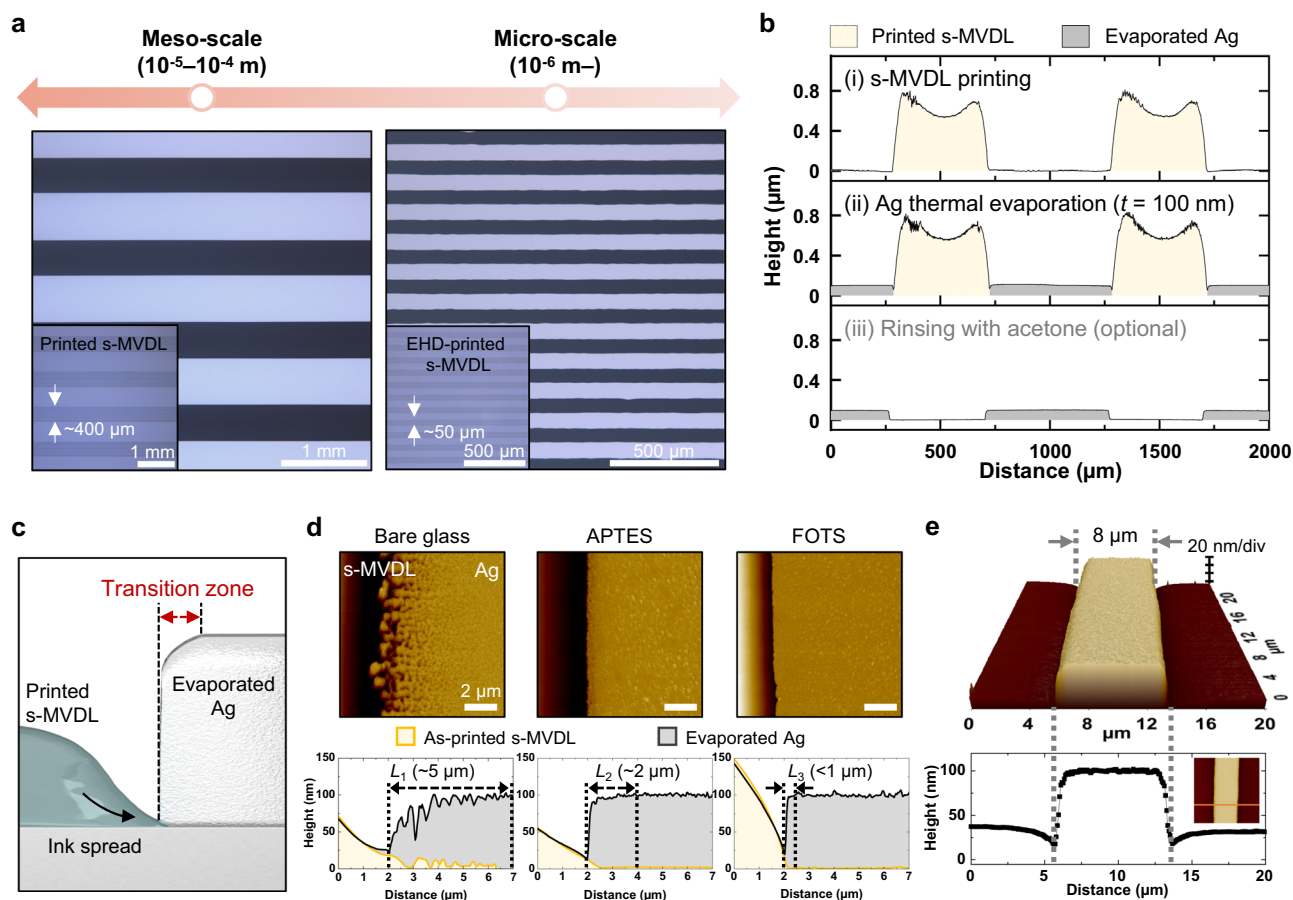


Fig. 3 | Printability, scalability, and fidelity of s-MVDL-assisted selective metal vapor deposition. **a** Optical microscopy images of patterned Ag thin films obtained using a pneumatic dispenser (left) and an EHD printer (right). The insets are the corresponding optical images of printed s-MVDL patterns. **b** Surface profiles after the sequential processes of s-MVDL printing, Ag thermal evaporation, and rinsing with acetone. **c** Schematic illustration of the transition zone formation at the

edge of printed s-MVDLs. **d** Surface topography images measured by AFM and the corresponding edge profiles after surface treatment with APTES and FOTS. **e** 3D surface topography image measured by AFM and the corresponding edge profile of the Ag thin film. A minimum feature size of $<8\ \mu\text{m}$ was achieved with the EHD-printed s-MVDL on the APTES-treated glass substrate.

linewidth of less than $8\ \mu\text{m}$ (Fig. 3e). For the patterned Ag thin films, an electrical conductivity of $\sim 4 \times 10^5\ \Omega^{-1}\ \text{cm}^{-1}$ and a surface roughness of $\sim 1.55\ \text{nm}$ were measured, which are comparable to those of thin Ag films deposited by a typical thermal evaporation process (Supplementary Fig. 15)³⁹. Therefore, we developed precisely patterned Ag thin films that can simultaneously provide superior electrical conductivity, low surface roughness, and sharp edge profiles through s-MVDL-assisted selective metal vapor deposition, which is promising for high-fidelity and high-resolution electrodes.

Selective metal vapor deposition on complex multi-curvature surfaces

Beyond planar substrates, a systematic framework for patterning onto curvilinear surfaces can significantly improve the functionality of thin metal films while fully exploiting their electro-optical and morphological advantages. The s-MVDL-based patterning method is highly compatible with various surfaces, including 3D form factors, due to the stretchability of the s-MVDL. When a tensile strain was applied to a free-standing s-MVDL using a universal testing machine (UTM), the s-MVDL could accommodate a strain of approximately 1000% without fracture, exhibiting superior mechanical durability (elongation at break $> 1000\%$) and low tensile stress ($< 0.4\ \text{MPa}$ under a tensile strain of 800%) (Supplementary Fig. 16). These results reveal the superior deformability of the s-MVDL, showing that it can compliantly stretch along with complex deformation of a substrate.

To investigate thin metal film patterning onto complex 3D surfaces, vacuum-forming of a thermoplastic sheet along 3D-printed bi-sinusoidal structures was introduced (Fig. 4a). A vacuum-forming process allows a thermoplastic sheet to be deformed along an arbitrary 3D structure when it is heated above the forming temperature^{40,41}. Herein, an underlying bi-sinusoidal structure with various non-developable curved surfaces in a unit cell, such as concave, convex, and saddle surfaces, was employed^{42,43}, thus providing greater structural complexity than previous research focused on single curved surfaces^{10,11,13}. The deformation compatibility of the printed s-MVDL was investigated using various bi-sinusoidal structures with design variables of pitch (P) and amplitude (A). The maximum tensile strain (ϵ_{max}) during the vacuum-forming process was determined to be approximately 100% for a geometric ratio ($2A/P$) of 1, which is within the allowable strain level for the s-MVDL (Supplementary Fig. 17). Therefore, the compliantly deformed s-MVDL along the bi-sinusoidal structures facilitated the formation of 3D-patterned Ag thin films with multi-curvatures (Supplementary Fig. 18). Although the maximum curvature and surface area increased as the geometric ratio increased, the resistance per unit area of $(0.23 \pm 0.01)\ \Omega\ \text{cm}^{-2}$ was maintained, clearly indicating that the Ag thin films were uniformly deposited even on the complex structures, regardless of the curvatures (Fig. 4b). The cross-sectional FE-SEM images also show the uniformly deposited Ag thin films along the various curvatures (Supplementary Fig. 19). Figure 4c shows an example of a 3D-patterned Ag thin film, where the

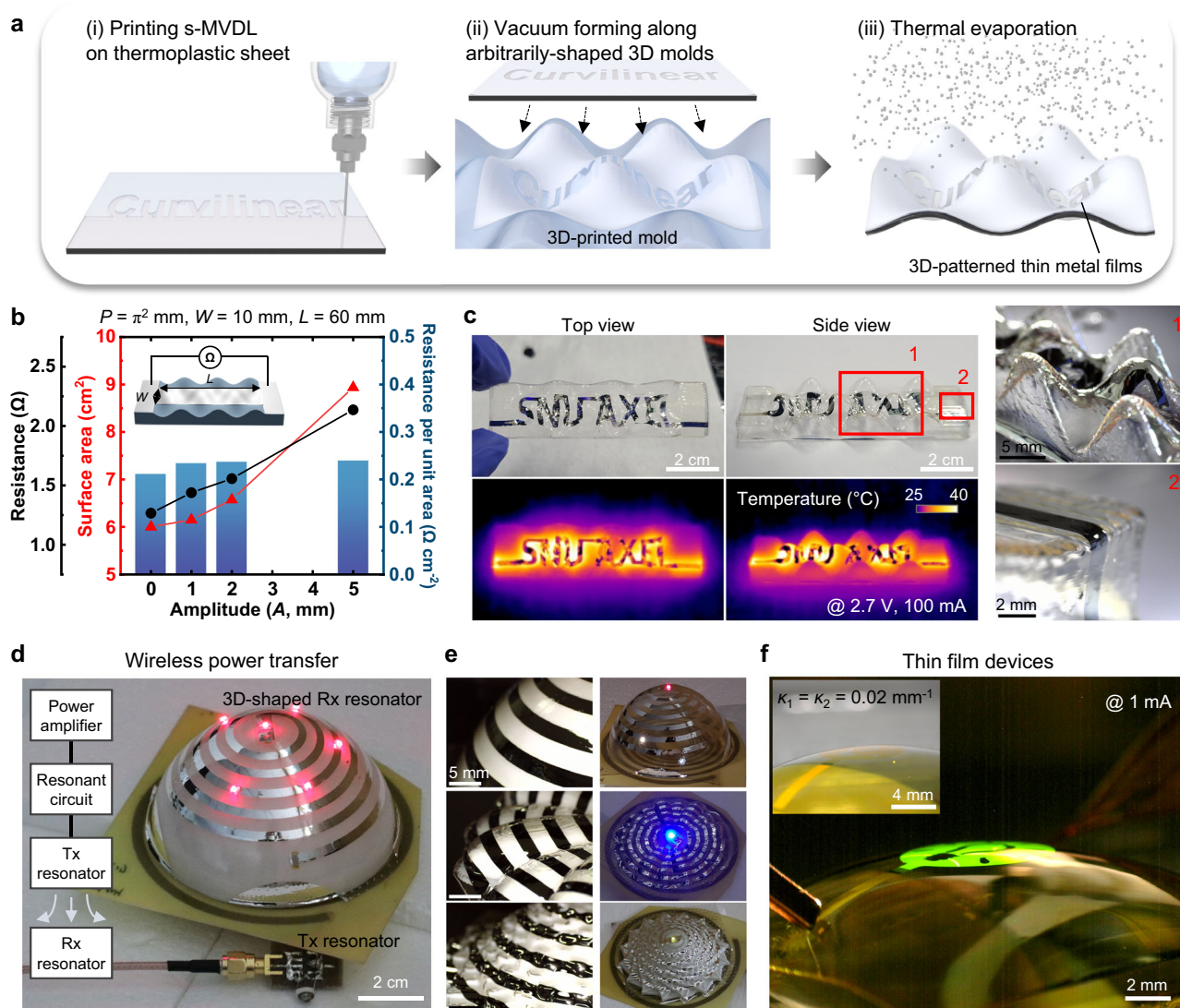


Fig. 4 | Selective metal vapor deposition on arbitrary 3D surfaces. **a** Schematic illustration of the s-MVDL-assisted thin metal film patterning process on 3D surfaces. **b** Electrical characterization of 3D-patterned metal electrodes on bi-sinusoidal surfaces with various amplitudes. The line and symbol plots represent the resistance and surface area, respectively, and the histogram represents the resistance per unit area. The inset shows a schematic illustration of the experimental setup for the resistance measurements. **c** Photograph of the 3D-patterned Ag thin films ($t = 100 \text{ nm}$) along bi-sinusoidal surface ($2A/P = 1$) with the letters ‘SNU AXEL’ and

the corresponding thermographic image visualizing the electrical connection along the 3D surface when biased at 2.7 V. **d** Photograph of the 3D-shaped spiral resonator fabricated using maskless patterning of Ag ($t = 300 \text{ nm}$) for wireless power transfer. **e** Photographs of 3D-shaped spiral resonators on various complex multi-curvature surfaces. **f** Photograph of a top-emitting OLED fabricated on a hemispherical surface ($\kappa_1 = \kappa_2 = 0.02 \text{ mm}^{-1}$) at a constant current bias of 1 mA. The inset shows a photograph of the OLED in the off-state.

letters ‘SNU AXEL’ were conformally deposited along a bi-sinusoidal surface, even including a steep slope. When an electrical bias was applied through both ends of the 3D-patterned Ag, a well-established electrical connection was identified along the curved surface using an IR camera, showing uniform thermal emission across the Ag film. While more complex 3D surfaces, including steep and shadowed areas, may reach coverage limits in our current experimental set-up, it is expected that applying additional strategies, such as a plane source, an inclined rotation, and metal-vapor integration method, can improve the deposition coverage on 3D surfaces^{17,24,44,45}.

To fully exhibit the potential of patterned thin-film electrodes on arbitrary shapes, a 3D metallic resonator for wireless power transfer and reflective bottom cathodes for thin-film devices were demonstrated. For wireless power transfer that delivers an induced electromotive force from the Tx resonator to the Rx resonator in the near-field range, a spiral-shaped power receiving resonator was designed on

a 3D curved surface (Fig. 4d and Supplementary Fig. 20)⁴⁶. LED chips were bonded to spiral-shaped Ag thin films to identify the power delivered to the 3D-patterned spiral resonator. As the 3D-patterned spiral resonator approached the planar-structured Tx resonator, the LED chips serially connected along the spiral-shaped Ag thin films emitted light, indicating successful power transfer to the 3D-patterned metallic resonator (Movie S1). Furthermore, 3D-patterned Ag thin films were deposited on complex multi-curvature surfaces. Regardless of the structural complexity of the 3D shapes, the Ag thin films were constructed without circuit disconnections and received sufficient power to illuminate the mounted LED chips (Fig. 4e and Supplementary Movie 1).

Thin-film-based LEDs, such as OLEDs, that can display information on curved surfaces are promising for use in automobiles and wearable devices⁷. However, their direct fabrication on non-developable curved surfaces remains challenging owing to the incompatibility of thin-film

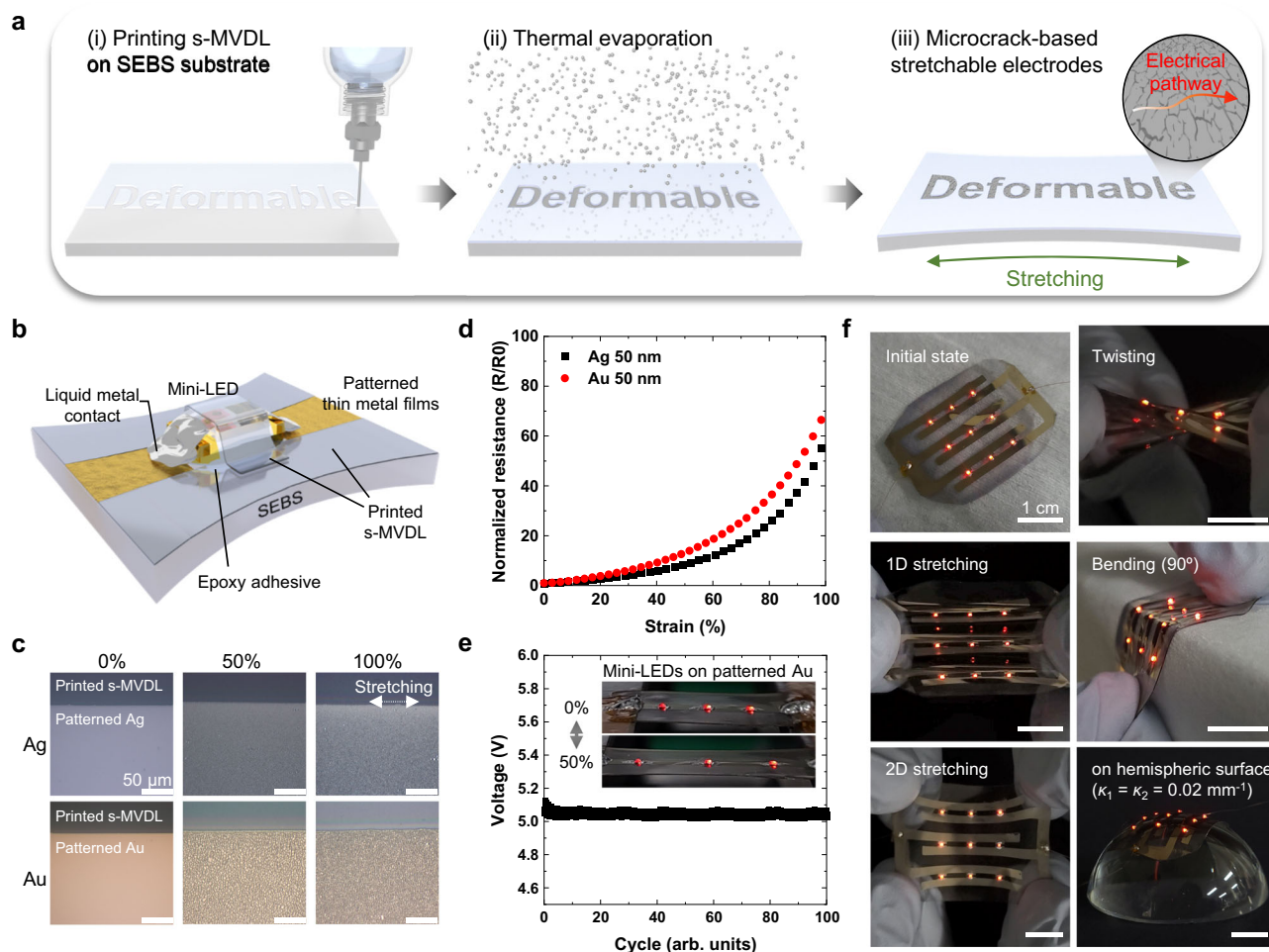


Fig. 5 | Selective metal vapor deposition for stretchable electrodes. **a** Schematic illustration of the s-MVDL-assisted thin metal film patterning process on a deformable substrate. **b** Schematic illustration of the stretchable LED structure. **c** Optical microscopy images of Ag and Au electrodes under uniaxial stretching of 0%, 50%, and 100%. **d** Electromechanical response of microcrack-based stretchable

thin metal films under uniaxial stretching up to 100%. **e** Cycle reliability of the stretchable LED array. Insets are photographs of stretchable LED arrays at strains of 0% and 50%. **f** Photographs of stretchable LED arrays driven by microcrack-based stretchable Au electrodes under various deformations.

patterning with curved surfaces. As selective metal vapor deposition enables direct patterning of thin metal films on 3D shapes, the fabrication of OLEDs on non-developable hemispherical surfaces could be demonstrated. A polyethylene naphthalate (PEN) sheet deformed along a hemisphere ($\kappa_1 = \kappa_2 = 0.02 \text{ mm}^{-1}$) was utilized as the substrate, and inverted, top-emitting OLEDs were fabricated on the Ag cathode patterned into a light bulb icon using an s-MVDL (Supplementary Fig. 21). In terms of the feasibility of the device structure, the OLED fabricated on a planar PEN substrate showed performance comparable to that of OLEDs fabricated on a glass substrate (Supplementary Fig. 22). The OLEDs fabricated on the hemispherical PEN substrate showed compliant light emission along the patterned light bulb on the curved surface (Fig. 4f and Supplementary Fig. 23).

In brief, s-MVDL-assisted selective deposition offers customizable, scalable patterning of thin metal films on arbitrary multi-curvature 3D surfaces, thus realizing the dimensional freedom of thin metal films. The combination of printing and thermal evaporation compensates for the limitations of previous techniques, thus ensuring high processability and throughput for high-fidelity thin metal films with superior conductivity and low surface roughness.

Selective metal vapor deposition for deformable electronics

In addition to s-MVDL-based 3D thin film circuits with fixed form, the softness of s-MVDLs implies they can be used to construct thermally

evaporated, stretchable circuits on deformable surfaces (Fig. 5a). While pure metal films lose their electrical conductivity at strains as low as a few percent^{47,48}, specific elastomeric substrate allow thin metal films to be electrically resilient under higher strains^{49–52}. As a deformable substrate, styrene-ethylene-butylene-styrene (SEBS), known to spontaneously form an interlocking structure with diffused metal atoms at a sufficiently low deposition rate, was employed. The robust interface allows the formation of microcracks under tensile strain while simultaneously preserving the electrical pathway. Therefore, the combination of SEBS, which promotes the diffusion of metal atoms, with a printed s-MVDL, which facilitates the desorption of metal vapor, makes it feasible to obtain readily patternable stretchable electrodes without the need for additional complex processes such as pre-stretching or stripping.

To explore the viability of s-MVDL-assisted selective deposition on deformable platforms, a stretchable inorganic LED array was fabricated by means of thin metal electrodes patterned using an s-MVDL (Fig. 5b). The s-MVDL ink exhibited favorable wetting on the SEBS substrate (contact angle $\sim 18^\circ$), showing strong affinity without requiring additional surface treatments (Supplementary Fig. 24). The stretchable LED array was composed of stretchable Au electrodes that reliably delivered electrical power and liquid metal solders that interfaced between the LED chips and the stretchable metal electrodes (Supplementary Fig. 25). To realize the proposed structure, a one-step

metallization was carried out on the SEBS substrate including LED chips and the printed s-MVDL. Notably, the metal film on the sides of the LED chips could serve as an adhesion layer for the liquid metal solder. Although liquid metal can offer a reliable electrical connection at the strain-concentrating interface owing to its fluidic nature at room temperature, its application in electronic devices is hindered by the surface tension induced by the formation of an oxide layer. However, the presence of a Au layer alleviates this issue, promoting wetting on LED chips and electrodes while simultaneously ensuring reliable electrical contact^{53,54}.

In typical thin metal films, large cracks running completely across the film are generated, leading to electrical failure even at a small strain (<2%)^{55,56}. On the other hand, the formation of microcracks in selectively deposited thin metal films using s-MVDLs implies that stretchability could be achieved without compromising the overall integrity and functionality (Fig. 5c). The softness of s-MVDL, characterized by low tensile stress under large deformation (<0.5 MPa @ tensile strain of 500%), has a negligible impact on the mechanical behavior of the stretchable system. When both Ag and Au films were uniaxially stretched up to 100%, microcracks evolved over the entire surface of the thin metal films. There was no noticeable delamination between the SEBS and s-MVDL, indicating synchronized movement of the s-MVDL under mechanical deformation. Even if delamination occurs in the s-MVDL, the electrical and mechanical performances of the system will remain stable because the substrate forms an interlocking structure with the electrodes and determines its strain distribution. Electrical characterization of the patterned thin metal films also revealed that the conductive pathway was maintained up to uniaxial stretching up to 100% (Fig. 5d). While the resistance increased with the applied strain, the electrical pathway remained through the anchored metal atoms in the SEBS matrix. The electromechanical response under stretching obtained in our study aligns with previous research⁵¹, exhibiting R/RO values of 8.67 for Ag and 13.1 for Au at a strain of 50%.

The fabricated LED array showed stable light emission under uniaxial stretching of 50% (Fig. 5e). Cyclic uniaxial stretching of 50% resulted in fluctuation in the driving voltage within 0.1 V, demonstrating stable operation with excellent mechanical stability. Furthermore, the stretchable LED array, extended to a 3 × 3 configuration, normally operated under various deformations, including uniaxial stretching, biaxial stretching, twisting, bending, or laminating over a hemispheric surface (Fig. 5f). This demonstration validates the reliability of our LED bonding scheme and microcrack-based stretchable metal electrodes, which can be readily obtained through s-MVDL-assisted selective metal vapor deposition. s-MVDLs could be seamlessly integrated on a deformable platform as a patterning agent without interfering with the behavior of the overall system. Their compatibility with deformable platforms opens up potential applications in customizable, large-area stretchable circuits, offering a more straightforward and practical method for enhanced processability.

Discussion

We reported the selective deposition of thin metal films by exploiting s-MVDLs as excellent metal-vapor-desorption layers. The highly mobile chain with low surface energy of e-PVDF-HFP serves as a key factor contributing to an ultralow condensation ratio (<2%). The metal vapor was predominantly repelled from the surface of the s-MVDLs during thermal evaporation, allowing the Ag-evaporated s-MVDLs to maintain their original optical transparency. The spatially patterned s-MVDLs facilitated the deposition of metal vapor only in the s-MVDL-free regions, thus enabling customizable and scalable patterning of thin metal films without compromising their conductivity and surface roughness. Furthermore, printed s-MVDLs with boundary thicknesses of less than tens of nanometers ensured that the edges of the patterned metal films were ultra-sharp, achieving a high-fidelity Ag thin film with a minimum transition zone (<1 μm) and a minimum feature

size (<8 μm). In addition to the desorption properties of the s-MVDL, its superior stretchability with a high elongation at break (>1000%) and low tensile stress (<0.4 MPa under a tensile strain of 800%) allowed compliant deformation along the substrate, resulting in 3D-patterned thin metal films on arbitrary shapes with multi-curvatures and microcrack-based stretchable thin metal films on elastomeric substrates. Our method offers a comprehensive framework for solving previous problems in patterning thin metal films, such as the tapered region from a shadow mask and its incompatibility with uneven shapes. Additional resources and complex post-processing, such as physical masks, etching, and lift-off processes, were not needed to establish complex circuits on unconventional surfaces, while the highly compatible desorption properties of the s-MVDLs with various metal atoms and substrates provided process universality. To fully exploit the thin metal films and their superior electro-optical characteristics, *in situ* selective deposition of thin metal films on curvilinear and deformable substrates was demonstrated through a 3D metallic resonator, top-emitting OLEDs, and a stretchable LED array, suggesting the feasibility of thin metal films for versatile soft electronics. For future research, improving the minimum feature size and pitch of thin metal films by further optimizing the printing parameters, exploring the detailed desorption mechanism according to the type of metal atoms, and extending circuit formation on a single plane to multilayered structures could be further investigated. The selective metal vapor deposition of complex circuits on arbitrary shapes can provide practical patterning solutions for various applications in soft electronics.

Methods

s-MVDL ink formulation

e-PVDF-HFP (G-8002, Daikin Corp.) was mixed with cross-linking agents of 1,3,5-triallyl-1,3,5-triazinane-2,4,6-trione (TAIC, Sigma-Aldrich Corp.) and dibenzoyl peroxide (BPO, Sigma-Aldrich Corp.) at a mass ratio of 20:1:1. The mixture was dissolved in PGMEA (Sigma-Aldrich Corp.) to obtain an e-PVDF-HFP concentration of 10 wt%. The prepared s-MVDL ink was stirred overnight before use. A concentration of 5 wt% was prepared separately for EHD printing. After spin-coating or direct writing the formulated s-MVDL ink, the deposited film is thermally cross-linked at 130 °C, although the thermal reaction is not necessarily required for desorption characteristics. During thermal cross-linking process, thermal energy decomposes the BPO leading to the generation of free radicals, which react with TAIC to form a covalent bond with e-PVDF-HFP, to achieve mechanical durability^{57–59}. The viscosity was measured using a rotational viscometer (LV DV2T with UL adapter, Brookfield), and the surface tension was measured by the ImageJ plugin using the pendant drop method.

Analysis of the desorption property of s-MVDL

The bare glass was sequentially cleaned with acetone and isopropyl alcohol (IPA) for 10 min each in an ultrasonic bath. After drying in an oven at 100 °C for 60 min, the substrates were used without additional surface treatment. c-PVDF-HFP (10 wt% in dimethyl sulfoxide, Sigma-Aldrich Corp.) was spin-coated at 1000 rpm on the bare glass and dried at 100 °C for 60 min. PDMS (Sylgard 184, Dow Corning Corp.) was mixed with cross-linking agents at a volume ratio of 10:1, and then diluted in hexane at a concentration of 10 wt%. The PDMS solution was spin-coated at 1000 rpm on the bare glass and cured at 60 °C for 4 h. FOTS (Thermo Fisher Corp.) was polymerized directly on the UV/O₃-treated glass, by immersing it in a glass chalet filled with toluene, followed by pipetting a FOTS solution at a concentration of 10 mg ml⁻¹. The sample remained inside the chalet for 30 min, during which the solution transitioned from transparent to slightly hazy state. Then, the glass sample was removed from the chalet and dried at 100 °C for 60 min. The s-MVDL ink (e-PVDF-HFP of 10 wt%) was spin-coated at 5000 rpm on the bare glass and cross-linked at 130 °C for 60 min. The

glass substrate coated with nothing, c-PVDF-HFP, PDMS, FOTS, and s-MVDL were simultaneously loaded into a vacuum chamber to deposit Ag thin films of the same thickness. Surface morphology of the samples was collected by AFM using a Bruker Icon Dimension instrument with a NSC19/AL-BS AFM probe (MikroMasch, Tallinn, Estonia nominal with a nominal spring constant of 0.5 N/m, resonance frequency of 60 kHz, and a tip radius of 5 nm). The scan resolution was set to 256×256 pixel with a scan rate of 0.6 Hz. The data was evaluated and depicted with Gwyddion SPM software. The optical transmittance was measured using a UV/Vis spectrometer (Lambda 35, PerkinElmer). The condensation coefficient was obtained from the EDS map spectrum measured by FE-SEM (JSM-7401F, JEOL) equipped with an EDS detector (X-Max, Oxford Instruments) at $\times 10,000$ magnification (spot size: $10 \times 7.5 \mu\text{m}$). The sheet resistance was measured using four-point probes spaced 1 mm apart connected with a source meter (Keithley 2400, Keithley).

s-MVDL printing and thermal evaporation

Printing of the s-MVDL ink was mainly conducted using a pneumatic dispenser (ML-808GX, Musashi Engineering Inc.) and a desktop robot (SHOT mini 200SX, Musashi Engineering Inc.). A syringe filled with the s-MVDL ink (e-PVDF-HFP of 10 wt%) was assembled with a 32 G needle (inner diameter = $100 \mu\text{m}$). Then, a pattern programmed by CAD software (MuCAD V, Musashi Engineering Inc.) was printed at an air pressure of 20 kPa and nozzle speed of 10 mm s^{-1} . An EHD printer (SIJ-050, SIJ Technology) was utilized to achieve smaller feature sizes. A nozzle with an inner diameter of $7 \mu\text{m}$ was filled with the s-MVDL ink (e-PVDF-HFP of 5 wt%), and a line array pattern was printed at a DC bias voltage of 0.6 kV, amplitude of 0.45 kV, pulse frequency of 100 Hz, and nozzle speed of 1 mm s^{-1} . The printed s-MVDL was cross-linked on a hot plate at $130 \text{ }^\circ\text{C}$ for 1 h and then placed in a thermal evaporator without mask alignment. Thermal evaporation proceeded once the vacuum level reached $<10^{-6}$ Torr. Then, metal pellets (Taewon Scientific Co.) were thermally evaporated by electrically heating a tungsten boat. The distance between the sample holder and metal source was maintained at -30 cm , and the sample holder was rotated at a constant speed of -80 rpm during thermal evaporation.

Surface treatment for optimization of the transition zone

Surface treatment for optimization of the transition zone was conducted using bare glass as the as-cleaned state. APTES (5 wt% in deionized water, Sigma-Aldrich Corp.) was drop-casted for 10 min on a UV/ O_3 -treated glass substrate, rinsed with deionized water for 1 min, and then sequentially blown with an N_2 gun. As-purchased FOTS was vaporized inside a vacuum desiccator for 10 min to modify the UV/ O_3 -treated glass substrates.

Thermoforming of s-MVDL-printed thermoplastic sheet for 3D electronics

Glycol-modified polyethylene terephthalate (PETG, 0.5T, Vaquform) and polyethylene naphthalate (PEN, Teonex Q65HA, Dupont Teijin) sheets were used as thermoformable substrates. The substrate was cut into squares of $13 \times 13 \text{ cm}$ to correspond to the size available for the vacuum former. The substrate was then gently cleaned with a wiper soaked in IPA and exposed to UV/ O_3 treatment for 5 min. UV/ O_3 treatment resulted in a transition zone width of less than $3 \mu\text{m}$, providing a clear edge profile (Supplementary Fig. 26). The s-MVDL ink was printed by a pneumatic dispenser on a UV/ O_3 -treated sheet. It should be noted that the process temperature was maintained below $50 \text{ }^\circ\text{C}$ for the PETG sheet owing to its thermal instability. The thermoplastic sheet with the printed s-MVDL was deformed into a 3D shape with a forming temperature of approximately $150 \text{ }^\circ\text{C}$ using a vacuum former (Easy-Vac2, 3 A Medes) along a 3D-printed mold fabricated by a fused deposition modeling (FDM)-type 3D printer (DP-200, Sindoh Co.). Finally, the 3D-shaped sheet with printed

s-MVDL was placed in a thermal evaporator, and metal evaporation was carried out.

Wireless power transfer using a 3D metallic resonator

The spiral-shaped resonator for wireless power transfer was patterned on a 3D curved surface using s-MVDL-assisted selective deposition. Spiral-shaped Ag thin films with a thickness of 300 nm, linewidth of 3 mm, pitch of 6 mm, and turn number of 5 were deposited on the 3D-shaped PETG substrate. Surface-mounted LED chips (red: LS-SPI70SR34-5, blue: LS-SPI72DNB74-5, green: LS-SPI70YG34-5, HSUKWANG) were assembled on a 3D-patterned Ag thin films using a conductive epoxy (CW2400, Chemtronics) curable at room temperature. Both ends of the spiral resonator were electrically connected using a jumper line of Cu wire. The wireless power transmission system consisted of a class D power amplifier (operating frequency: 6.78 MHz monotone), resonant capacitor, and planar Tx resonator, powered by a DC power of 12 V. The AC power of the power amplifier was modulated to 0.2 mW to drive single blue/green LEDs, 0.9 mW to drive a single red LED (Fig. 4e), and 3.2 W to drive multiple red LEDs (Fig. 4d). The AC power was measured using a power meter (HP 437B, Hewlett-Packard).

Fabrication of curved OLEDs on the 3D surface

Inverted and top-side emitting OLEDs were fabricated using thin metal electrodes. A PEN substrate with printed s-MVDL was prepared and deformed into a hemispherical shape. For the electrical characterization of the fabricated OLED structure, OLEDs on planar glass and PEN substrates were prepared separately. After printing the s-MVDL under ambient conditions, other processes for depositing electrodes or active layers were performed inside an Ar-filled glove box. The bottom cathode of Ag ($t = 100 \text{ nm}$) was patterned using s-MVDL-assisted selective metal vapor deposition, while the samples for electrical characterization used shadow masks to pattern the metal electrodes. The electron injection layer of zinc oxide nanoparticles (ZnO, 10:1 diluted in volume with butanol, N-13, Avantama) was spin-coated at 4000 rpm and dried at $100 \text{ }^\circ\text{C}$ for 10 min. Polyethylenimine (PEI, 0.1 wt % in IPA, Sigma-Aldrich) was spin-coated at 1000 rpm and dried at $100 \text{ }^\circ\text{C}$ for 10 min. Subsequently, the PEI layer was rinsed with ethanol by spin-coating at 4000 rpm and then dried at $100 \text{ }^\circ\text{C}$ for 10 min. The emission layer of super yellow (SY, 0.6 wt% in toluene, PDY-132, Merck) was spin-coated at 2000 rpm and dried at $90 \text{ }^\circ\text{C}$ for 1 h. The sample was then placed in a thermal evaporator after covering only the contact point of the bottom cathode with Al foil. The hole injection layer of molybdenum trioxide (MoO_3 , Taewon Scientific Co., $t = 10 \text{ nm}$) and top anode of ultrathin Ag ($t = 20 \text{ nm}$) were sequentially evaporated. Finally, only the OLEDs for electrical characterization were encapsulated by attaching a glass lid using a UV-curable epoxy (XNR5570, Nagase ChemteX Corp.) to protect them from ambient conditions. The J - V - L characteristics of the OLED were measured using a spectrometer (CS-2000, Konica Minolta), digital multimeter (Keithley 2000, Keithley), and source-measurement unit (Keithley 237, Keithley) by sweeping the voltage at intervals of 0.1 V.

Stretchable thin metal electrodes on SEBS substrate

Styrene-ethylene-butylene-styrene block copolymer (SEBS, Tuftec HI062, Asahi Kasei) was used as an elastomeric substrate. A SEBS solution dissolved in toluene at a concentration of 100 mg ml^{-1} was drop-casted onto a FOTS-treated glass, and dried overnight at room temperature. The fully dried SEBS substrate was used without any additional thermal or surface treatment. Subsequently, the s-MVDL ink was printed onto the SEBS substrate to define the areas where thin metal films would not be deposited. The printed s-MVDL was annealed on a hot plate at $100 \text{ }^\circ\text{C}$. The SEBS substrate with printed s-MVDL was then transferred to the thermal evaporator. Thermal evaporation of metal sources (Ag or Au) was conducted at a deposition rate of $0.5 \text{ } \text{Å s}^{-1}$ and a deposition thickness of 50 nm.

Fabrication of stretchable LED array

The s-MVDL ink was printed onto a SEBS substrate to designate the deposition region for thin metal films, followed by drying at 100 °C for 60 min. Then, LED chips (SML-P11UT, Rohm Semiconductor) were bonded onto the epoxy adhesive (DX-20C, Loctite) printed on SEBS substrate. The epoxy adhesive was cured in an oven at 150 °C for 60 min. Subsequently, the s-MVDL was additionally printed above the LED package along the arch-shaped trajectory to cover between the anode and cathode of the LED chips. It prevents electrical shorts between the anode and cathode and opens up a window for the light-emitting side. Finally, Au was thermally evaporated, thus resulting in selective deposition on two regions; (i) the exposed SEBS region, forming stretchable metal interconnects to drive the LED chips, and (ii) the sides of LED chips where the anode and cathode were located. The 3D-deposited Au films on the sides of LED chips served as an adhesion layer for liquid metal solders (Gallium–Indium eutectic, Sigma-Aldrich Corp.), providing improved wetting and reliable electrical contact.

Characterization

The map spectrum of the atomic components was analyzed using FE-SEM (Sigma 300, ZEISS) equipped with an EDS detector (XFlash 6160, Bruker). The dark dots in Fig. 1b are due to the limitations of the thickness resolution and finite processing time of the EDS analysis. Optical images were obtained using a digital microscope (DSX510, Olympus Corp.) and a handheld digital microscope (AM4515T, AnMo Electronics Corp.). The surface profiles were measured using a stylus profilometer (DektakXT-A, Bruker) and AFM (XE-150, Parks Systems Corp.). The stress–strain curves were obtained using a UTM (Instron 5543, Instron Corp.) at a constant speed of 100 mm min⁻¹. Finite element method (FEM) simulations were performed to determine the principal strain induced during the vacuum-forming process using the structural module of COMSOL Multiphysics. IR thermographic imaging was performed using an IR camera (T420, Teledyne FLIR). The resistance on the 3D bi-sinusoidal surfaces was measured by the four-wire sensing mode of a source meter (Keithley 2400, Keithley).

Data availability

The authors declare that all data supporting the findings of this study are available within the article and its Supplementary Information. Source data are provided with this paper.

References

- Lee, G.-H. et al. Multifunctional materials for implantable and wearable photonic healthcare devices. *Nat. Rev. Mater.* **5**, 149–165 (2020).
- Jinno, H. et al. Self-powered ultraflexible photonic skin for continuous bio-signal detection via air-operation-stable polymer light-emitting diodes. *Nat. Commun.* **12**, 2234 (2021).
- Niu, S. et al. A wireless body area sensor network based on stretchable passive tags. *Nat. Electron.* **2**, 361–368 (2019).
- Kim, T. Y. et al. Wireless theranostic smart contact lens for monitoring and control of intraocular pressure in glaucoma. *Nat. Commun.* **13**, 6801 (2022).
- Gao, X. et al. A photoacoustic patch for three-dimensional imaging of hemoglobin and core temperature. *Nat. Commun.* **13**, 7757 (2022).
- Choi, C. et al. Curved neuromorphic image sensor array using a mos2-organic heterostructure inspired by the human visual recognition system. *Nat. Commun.* **11**, 5934 (2020).
- Huang, Y. et al. Assembly and applications of 3d conformal electronics on curvilinear surfaces. *Mater. Horiz.* **6**, 642–683 (2019).
- Hora, J., Hall, C., Evans, D. & Charrault, E. Inorganic thin film deposition and application on organic polymer substrates. *Adv. Eng. Mater.* **20**, 1700868 (2018).
- Lu, X., Zhang, Y. & Zheng, Z. Metal-based flexible transparent electrodes: Challenges and recent advances. *Adv. Electron. Mater.* **7**, 2001121 (2021).
- Cai, H. et al. Utilization of resist stencil lithography for multi-dimensional fabrication on a curved surface. *ACS Nano* **12**, 9626–9632 (2018).
- Kim, J.-H., Hong, S. H., Seong, K.-D. & Seo, S. Fabrication of organic thin-film transistors on three-dimensional substrates using free-standing polymeric masks based on soft lithography. *Adv. Funct. Mater.* **24**, 2404–2408 (2014).
- Park, T. H., Kim, J. H. & Seo, S. Facile and rapid method for fabricating liquid metal electrodes with highly precise patterns via one-step coating. *Adv. Funct. Mater.* **30**, 2003694 (2020).
- Paik, S. et al. Near-field sub-diffraction photolithography with an elastomeric photomask. *Nat. Commun.* **11**, 805 (2020).
- Yang, Q. et al. High-speed, scanned laser structuring of multi-layered eco/bioresorbable materials for advanced electronic systems. *Nat. Commun.* **13**, 6518 (2022).
- Sun, J. et al. Fabricating high-resolution metal pattern with inkjet printed water-soluble sacrificial layer. *ACS Appl. Mater. Interfaces* **12**, 22108–22114 (2020).
- Tsuijoka, T. Selective metal-vapor deposition on organic surfaces. *Chem. Rec.* **16**, 231–248 (2016).
- Tsuijoka, T., Shirakawa, R., Matsumoto, S., Nishimura, R. & Uchida, K. Metal-vapor integration/transportation based on metal-atom desorption from polymer surfaces with a low glass-transition temperature. *J. Vac. Sci. Technol. A* **35**, 020603 (2017).
- Tsuijoka, T. & Nishimura, A. Selective noble-metal deposition modulation on photocurable polydimethylsiloxane films for electronics device applications. *Appl. Phys. A* **127**, 228 (2021).
- Varagnolo, S., Lee, J., Amari, H. & Hatton, R. A. Selective deposition of silver and copper films by condensation coefficient modulation. *Mater. Horiz.* **7**, 143–148 (2020).
- Bellchambers, P. et al. High performance transparent silver grid electrodes for organic photovoltaics fabricated by selective metal condensation. *Adv. Mater.* **35**, 2300166 (2023).
- Lee, J., Varagnolo, S., Walker, M. & Hatton, R. A. Transparent fused nanowire electrodes by condensation coefficient modulation. *Adv. Funct. Mater.* **30**, 2005959 (2020).
- Varagnolo, S., Park, K.-W., Lee, J.-K. & Hatton, R. A. Embedded-grid silver transparent electrodes fabricated by selective metal condensation. *J. Mater. Chem. C* **8**, 13453–13457 (2020).
- Tsuijoka, T. Metal-pattern preparation based on selective deposition using soft organofluorine surfaces. *J. Vac. Sci. Technol. B* **41**, 052209 (2023).
- Tsuijoka, T. & Kusaka, H. Metal atom desorption from organofluorine surfaces: What factors govern desorption? *Adv. Mater. Interfaces* **9**, 2201096 (2022).
- Faupel, F., Zaporozhchenko, V., Thran, A., Strunskus, T. & Kiene, M. in *Diffusion processes in advanced technological materials* (ed. Gupta, D.) 333–363 (William Andrew Inc., 2005).
- Tsuijoka, T. et al. Surface molecular kinetics on the outermost layer characterized by nucleation of mg-vapor atoms. *Appl. Surf. Sci.* **490**, 309–317 (2019).
- Wang, C. et al. Significance of the double-layer capacitor effect in polar rubbery dielectrics and exceptionally stable low-voltage high transconductance organic transistors. *Sci. Rep.* **5**, 17849 (2015).
- Yang, Y. et al. Perturbing effects of bulky comonomers on the chain conformation of poly (vinylidene fluoride). *Polymer* **49**, 1926–1933 (2008).
- Cao, Y. et al. A highly stretchy, transparent elastomer with the capability to automatically self-heal underwater. *Adv. Mater.* **30**, 1804602 (2018).
- Cao, Y. et al. Self-healing electronic skins for aquatic environments. *Nat. Electron.* **2**, 75–82 (2019).

31. Shah, A. A. et al. Origin of fluoropolymer affinity toward water and its impact on membrane performance. *ACS Appl. Polym. Mater.* **2**, 5249–5258 (2020).
32. Oh, M.-K. et al. Morphological and sers properties of silver nanorod array films fabricated by oblique thermal evaporation at various substrate temperatures. *Nanoscale Res. Lett.* **10**, 259 (2015).
33. Yang, M.-C. et al. Reproducible sers substrates manipulated by interparticle spacing and particle diameter of gold nano-island array using in-situ thermal evaporation. *Spectrochim. Acta A* **303**, 123190 (2023).
34. Esa, Z., Abid, M., Zaini, J. H., Aissa, B. & Nauman, M. M. Advancements and applications of electrohydrodynamic printing in modern microelectronic devices: A comprehensive review. *Appl. Phys. A* **128**, 780 (2022).
35. Vazquez-Mena, O. et al. Analysis of the blurring in stencil lithography. *Nanotechnology* **20**, 415303 (2009).
36. Wang, Z. et al. Angled physical vapor deposition techniques for non-conformal thin films and three-dimensional structures. *MRS Commun.* **6**, 17–22 (2016).
37. Liu, K. et al. Efficient investigation of high-performance perovskite solar cells based on shadow-mask kits with uniform patterning and antishadowing capabilities. *Adv. Mater. Technol.* **6**, 2001207 (2021).
38. Kim, C. et al. Fine metal mask material and manufacturing process for high-resolution active-matrix organic light-emitting diode displays. *J. Soc. Inf. Disp.* **28**, 668–679 (2020).
39. Xie, Y., Ouyang, S., Wang, D., Lee, W.-Y. & Fong, H. H. Highly smooth and conductive silver film with metallo-organic decomposition ink for all-solution-processed flexible organic thin-film transistors. *J. Mater. Sci.* **55**, 15908–15918 (2020).
40. Hong, F., Tendra, L., Myant, C. & Boyle, D. Vacuum-formed 3d printed electronics: Fabrication of thin, rigid and free-form inter-active surfaces. *SN Comput. Sci.* **3**, 275 (2022).
41. Choi, J. et al. Customizable, conformal, and stretchable 3d electronics via predistorted pattern generation and thermoforming. *Sci. Adv.* **7**, eabj0694 (2021).
42. Rich, S. I., Lee, S., Fukuda, K. & Someya, T. Developing the non-developable: Creating curved-surface electronics from non-stretchable devices. *Adv. Mater.* **34**, 2106683 (2022).
43. Xiao, L., Cheng, M., Chen, F., Jiang, S. & Huang, Y. Theoretical modeling of conformal criterion for flexible electronics attached onto complex surface. *J. Appl. Mech.* **89**, 031005 (2022).
44. Hwang, C., Kim, S. S. & Chin, B. D. P-49: Ultimate solution: The belt plane source evaporators for future amoled and qd oled tv. *SID Symp. Dig. Tech. Pap.* **51**, 1530–1533 (2020).
45. Arscott, S. On evaporation via an inclined rotating circular lift-off shadow or stencil mask. *J. Vac. Sci. Technol. B* **37**, 011602 (2019).
46. Kim, J., Cha, C., Oh, J. & Hong, Y. New design topology of high-q factor printed base antenna having unequal width and pitch used for near-field wireless power transmission. *IEEE J. Emerg. Sel. Top. Power Electron.* **10**, 984–996 (2022).
47. Kim, J.-H. et al. Tensile testing of ultra-thin films on water surface. *Nat. Commun.* **4**, 2520 (2013).
48. Li, T. & Suo, Z. Ductility of thin metal films on polymer substrates modulated by interfacial adhesion. *Int. J. Solids Struct.* **44**, 1696–1705 (2007).
49. Chae, S. et al. Kinetically controlled metal-elastomer nanophases for environmentally resilient stretchable electronics. *Nat. Commun.* **15**, 3071 (2024).
50. Jiang, Y. et al. A universal interface for plug-and-play assembly of stretchable devices. *Nature* **614**, 456–462 (2023).
51. Lee, Y. et al. Standalone real-time health monitoring patch based on a stretchable organic optoelectronic system. *Sci. Adv.* **7**, eabg9180 (2021).
52. Matsuhisa, N. et al. High-transconductance stretchable transistors achieved by controlled gold microcrack morphology. *Adv. Electron. Mater.* **5**, 1900347 (2019).
53. Livshits, G. I. et al. Sacrificial gold coating enhances transport of liquid metal in pressurized fountain pen lithography. *Sci. Rep.* **11**, 4670 (2021).
54. Zhu, H. et al. Fully solution processed liquid metal features as highly conductive and ultrastretchable conductors. *npj Flex. Electron.* **5**, 25 (2021).
55. Cho, C. et al. Strain-resilient electrical functionality in thin-film metal electrodes using two-dimensional interlayers. *Nat. Electron.* **4**, 126–133 (2021).
56. Seghir, R. & Arscott, S. Controlled mud-crack patterning and self-organized cracking of polydimethylsiloxane elastomer surfaces. *Sci. Rep.* **5**, 14787 (2015).
57. Lu, C., Lee, W.-Y., Shih, C.-C., Wen, M.-Y. & Chen, W.-C. Stretchable polymer dielectrics for low-voltage-driven field-effect transistors. *ACS Appl. Mater. Interfaces* **9**, 25522–25532 (2017).
58. Shih, C. C., Lee, W. Y., Lu, C., Wu, H. C. & Chen, W. C. Enhancing the mechanical durability of an organic field effect transistor through a fluoroelastomer substrate with a crosslinking-induced self-wrinkled structure. *Adv. Electron. Mater.* **3**, 1600477 (2017).
59. Seo, J., Ha, J., Lee, B., Kim, H. & Hong, Y. Fluoroelastomer encapsulation for enhanced reliability of solution-processed carbon nanotube thin-film transistors. *Thin Solid Films* **704**, 138021 (2020).

Acknowledgements

This research was supported by National R&D Program through the National Research Foundation of Korea(NRF) funded by Ministry of Science and ICT(2020M3D1A2101801, RS-2024-00416978).

Author contributions

S.J. and H.Y. designed and carried out the overall experiments. L.F.M. conducted AFM measurement for mapping of surface morphology. G.K. conducted EHD printing. J.K. designed the wireless power transfer system. J.S. conducted UTM measurement. D.K. and H.P. contributed to the OLED fabrication. S.J. and H.Y. performed data analysis, organized the data and write the manuscript. B.L. contributed to the material analysis and discussion of results. Y.H. supervised the project. All the authors reviewed and edited the manuscript.

Competing interests

S.J., H.Y., and Y.H. have been named as inventors in a pending patent application submitted by Seoul National University R&DB Foundation (Korea patent application number KR 10-2022-0093976, 28 July 2022; KR 10-2023-0088330, 7 July 2023; KR 10-2023-0099666, 31 July 2023). The remaining authors declare no competing interests.

Additional information

Supplementary information The online version contains supplementary material available at <https://doi.org/10.1038/s41467-024-51585-2>.

Correspondence and requests for materials should be addressed to Byeongmoon Lee or Yongtaek Hong.

Peer review information *Nature Communications* thanks Tsuyoshi Tsujioaka, and the other, anonymous, reviewer(s) for their contribution to the peer review of this work. A peer review file is available.

Reprints and permissions information is available at <http://www.nature.com/reprints>

Publisher's note Springer Nature remains neutral with regard to jurisdictional claims in published maps and institutional affiliations.

Open Access This article is licensed under a Creative Commons Attribution-NonCommercial-NoDerivatives 4.0 International License, which permits any non-commercial use, sharing, distribution and reproduction in any medium or format, as long as you give appropriate credit to the original author(s) and the source, provide a link to the Creative Commons licence, and indicate if you modified the licensed material. You do not have permission under this licence to share adapted material derived from this article or parts of it. The images or other third party material in this article are included in the article's Creative Commons licence, unless indicated otherwise in a credit line to the material. If material is not included in the article's Creative Commons licence and your intended use is not permitted by statutory regulation or exceeds the permitted use, you will need to obtain permission directly from the copyright holder. To view a copy of this licence, visit <http://creativecommons.org/licenses/by-nc-nd/4.0/>.

© The Author(s) 2024